

Hints for a gravitational constant transition in Tully-Fisher data

George Alestas ¹,^{*}Ioannis Antoniou ¹,[†]Leandros Perivolaropoulos ¹,[‡]

¹*Department of Physics, University of Ioannina, GR-45110, Ioannina, Greece*

27 July 2022

ABSTRACT

We use an up to date compilation of Tully-Fisher data to search for transitions in the evolution of the Tully-Fisher relation. Using a recently published data compilation, we find hints at $\approx 3\sigma$ level for a transition at a critical distance $D_c \approx 17Mpc$. The zero point (intercept) amplitude of the transition is $\Delta \log A_B \approx 0.2 \pm 0.06$ while the slope remains practically unchanged. If the transition is interpreted as due to a gravitational strength transition, it would imply a shift of the effective gravitational constant to lower values for distances larger than $D_c \approx 17Mpc$ by $\frac{\Delta G}{G} = -0.1 \pm 0.03$. Such a shift is of the anticipated sign and magnitude but at somewhat lower distance (redshift) than the gravitational transition recently proposed to address the Hubble and growth tensions ($\frac{\Delta G}{G} \approx -0.1$ at transition redshift $z_t \lesssim 0.01$ ($D_c \lesssim 40Mpc$)).

Key words: Tully Fisher – Newton Constant – Hubble tension

1 INTRODUCTION

The Tully–Fisher relation (TFR) (Tully & Fisher 1977) has been proposed as an empirical relation that connects the intrinsic optical luminosity of spiral galaxies with their observed maximum velocity v_{rot} in the rotation curve as

$$L = Av_{rot}^s \quad (1)$$

where $s \approx 4$ is the slope in a logarithmic plot of (1) and A is a constant ($\log(A)$ is the zero point or intercept). The constants s and A appear to depend very weakly on galaxy properties including the mass to light ratio, the observed surface brightness, the galactic profiles, HI gas content, size, *etc.* (Lelli et al. 2016). They clearly also depend however on the fundamental properties of gravitational interactions as demonstrated below.

The baryonic Tully-Fisher relation (BTFR) is similar to eq. (1) but connects the galaxy’s total baryonic mass (the sum of mass in stars and HI gas) M_B with the rotation velocity as

$$M_B = A_B v_{rot}^s \quad (2)$$

where $A_B \approx 50M_\odot km^{-4} s^4$ (McGaugh 2005). This allows to include gas rich dwarf galaxies which appear in groups and have stellar masses below $10^9 M_\odot$.

A simple heuristic analytical derivation for the BTFR can be obtained as follows (Aaronson et al. 1979). Consider a star in a circular orbit of radius R around a galactic mass M rotating with velocity v . Then

$$v^2 = G_{\text{eff}} M/R \implies v^4 = (G_{\text{eff}} M/R)^2 \sim M S G_{\text{eff}}^2 \quad (3)$$

where G_{eff} is the effective Newton’s constant involved in gravitational interactions and S the surface density $S \equiv M/R^2$ which is expected

to be constant (Freeman 1970). From eqs. (2) and (3) it is anticipated that

$$A_B \sim G_{\text{eff}}^{-2} S^{-1} \quad (4)$$

Therefore the BTFR can in principle probe both galaxy formation dynamics (through *e.g.* S) and possible fundamental constant dynamics (through G_{eff}). An interesting feature of the BTFR is that despite of the above heuristic derivation, it appears to be robust even in cases when the galaxy sample includes low S and/or varying S galaxies (Zwaan et al. 1995; McGaugh & de Blok 1998). In fact no other parameter appears to be significant in the BTFR.

The BTFR has been shown to have lower scatter (Lelli et al. 2016) than the classic stellar TFR and also to be applicable for galaxies with stellar masses lower than $10^9 M_\odot$. It is also more robust than the classic TFR (Freeman 1999; McGaugh et al. 2000; Verheijen 2001; Zaritsky et al. 2014) since the parameters A_B (intercept) and s are very weakly dependent on galactic properties such as size and surface brightness (Lelli et al. 2019).

The low scatter of the BTFR and its robustness make it useful as a distance indicator for the measurement of the Hubble constant H_0 . A calibration of the BTFR using Cepheid and TRGB distances has lead to a value of $H_0 = 75 \pm 3.8 km s^{-1} Mpc^{-1}$ (Schombert et al. 2020).

This value of H_0 is consistent with local measurements of H_0 using SnIa calibrated with Cepheids ($H_0 = 73.2 \pm 1.3 km s^{-1} Mpc^{-1}$) (Riess et al. 2021) but is in tension with the value of H_0 obtained using the early time sound horizon standard ruler calibrated using the CMB anisotropy spectrum in the context of the standard Λ CDM model ($H_0 = 67.36 \pm 0.54 km s^{-1} Mpc^{-1}$) (Aghanim et al. 2020). The tension between the CMB and Cepheid calibrators is at level larger than 4σ and constitutes a major problem for modern cosmologies (for a recent review and approaches see Refs. (Di Valentino et al. 2021; Alestas et al. 2020b; Alestas & Perivolaropoulos 2021)).

The Hubble tension may also be viewed as an inconsistency between the value of the standardized SnIa absolute magnitude M calibrated using Cepheids in the redshift range $0 < z < 0.01$ (distance

* Contact e-mail: g.alestas@uoi.gr

† Contact e-mail: i.antoniou@uoi.gr

‡ Contact e-mail: leandros@uoi.gr

Method	$\frac{\Delta G_{\text{eff}}}{G_{\text{eff}}} _{\text{max}}$	$\frac{G_{\text{eff}}}{G_{\text{eff}}} _{\text{max}}$ (yr^{-1})	time scale (yr)	References
Lunar ranging		1.47×10^{-13}	24	(Hofmann & Müller 2018)
Solar system		7.8×10^{-14}	50	(Pitjeva & Pitjev 2013)
Pulsar timing		3.1×10^{-12}	1.5	(Deller et al. 2008)
Orbits of binary pulsar		1.0×10^{-12}	22	(Zhu et al. 2019)
Ephemeris of Mercury		4×10^{-14}	7	(Genova et al. 2018)
Exoplanetary motion		10^{-6}	4	(Masuda & Suto 2016)
Hubble diagram Smla	0.1	1×10^{-11}	$\sim 10^8$	(Gaztañaga et al. 2009)
Pulsating white-dwarfs		1.8×10^{-10}	0	(Córscico et al. 2013)
Viking lander ranging		4×10^{-12}	6	(Hellings et al. 1983)
Helioseismology		1.6×10^{-12}	4×10^9	(Guenther et al. 1998)
Gravitational waves	8	5×10^{-8}	1.3×10^8	(Vijaykumar et al. 2020)
Paleontology	0.1	2×10^{-11}	4×10^9	(Uzan 2003)
Globular clusters		35×10^{-12}	$\sim 10^{10}$	(Degl'Innocenti et al. 1996)
Binary pulsar masses		4.8×10^{-12}	$\sim 10^{10}$	(Thorsett 1996)
Gravitochemical heating		4×10^{-12}	$\sim 10^8$	(Jofre et al. 2006)
Big Bang Nucleosynthesis*	0.05	4.5×10^{-12}	1.4×10^{10}	(Alvey et al. 2020)
Anisotropies in CMB*	0.095	1.75×10^{-12}	1.4×10^{10}	(Wu & Chen 2010)

Table 1. Solar system, astrophysical and cosmological constraints on the evolution of the gravitational constant. Methods with star (*) constrain G_N while the rest constrain G_{eff} . The latest and strongest constraints are shown for each method.

ladder calibration) and the corresponding M value calibrated using the recombination sound horizon (inverse distance ladder calibration) for $0.01 < z < z_{\text{rec}}$. Thus, a recently proposed class of approaches to the resolution of the Hubble tension involves a transition (Marra & Perivolaropoulos 2021; Alestas et al. 2020a) of the standardized intrinsic Smla luminosity L and absolute magnitude M at a redshift $z_t \approx 0.01$ from $M = (-19.24 \pm 0.037) \text{ mag}$ for $z < z_t$ (as implied by Cepheid calibration) to $M = (-19.4 \pm 0.027) \text{ mag}$ (as implied by CMB calibration of the sound horizon at decoupling) (Camarena & Marra 2020). Such a transition may occur due to a transition of the strength of the gravitational interactions G_{eff} which modifies the Smla intrinsic luminosity L by changing the value of the Chandrasekhar mass. The simplest assumption leads to $L \sim M_{Ch} \sim G_{\text{eff}}^{-3/2}$ (Amen-dola et al. 1999; Gaztanaga et al. 2002) even though corrections may be required to the above simplistic approach (Wright & Li 2018).

The weak evolution and scatter of the BTFR can be used as a probe of galaxy formation models as well as a probe of possible transitions of fundamental properties of gravitational dynamics since the zero point constant A_B is inversely proportional to the square of the gravitational constant G . Previous studies investigating the evolution of the best fit zero point $\log A_B$ and slope s of the BTFR have found a mild high z evolution of the zero point from $z \approx 0.9$ to $z \approx 2.3$ (Übler et al. 2017) which was attributed to the galactic evolution inducing lower gas fraction at low redshifts after comparing with the corresponding evolution of the stellar TFR (STFR) which ignores the contribution of gas in the galactic masses.

Ref. (Übler et al. 2017) and other similar studies assume a fixed strength of fundamental gravitational interactions and make no attempt to search for sharp features in the evolution of the zero point. In addition, they focus on comparison of high redshift with low redshift effects without searching for possible transitions within the low z spiral galaxy data. Such transitions if present would be washed out and hidden from these studies due to averaging effects. In the present analysis we search for transition effects in the BTFR at $z \lesssim 0.01$ (distances $D \lesssim 40 Mpc$) which may be due to either astrophysical mechanisms or to a rapid transition of the strength of the gravitational interactions G_{eff} due to fundamental physics.

In many modified gravity theories including scalar tensor theories the strength of gravitational interactions G_{eff} measured in

Cavendish type experiments measuring force F between masses ($F = G_{\text{eff}} \frac{m_1 m_2}{r^2}$), is distinct from the Planck mass corresponding to G_N that determines the cosmological background expansion rate ($H^2 = \frac{8\pi G_N}{3} \rho_{\text{tot}}$).

For example, in scalar tensor theories involving a scalar field ϕ and a non-minimal coupling $F(\phi)$ of the scalar field to the Ricci scalar in the Lagrangian, the gravitational interaction strength is (Esposito-Farese & Polarski 2001)

$$G_{\text{eff}} = \frac{1}{F} \frac{2F + 4F_{,\phi}^2}{2F + 3F_{,\phi}^2} \quad (5)$$

while the Planck mass related G_N is

$$G_N = \frac{1}{F} \quad (6)$$

Most current astrophysical and cosmological constraints on Newton's constant, constrain either the time derivative of G_{eff} at specific times, or assume a smooth power-law evolution of G_{eff} or constrain changes of the Planck mass related G_N instead of G_{eff} (CMB and Nucleosynthesis constraints (Alvey et al. 2020)). Therefore, these studies are less sensitive in the detection of rapid transitions of G_{eff} at low z .

The current constraints on the evolution of G_{eff} and G_N are summarized in Table 1 where we review the experimental constraints from local and cosmological time scales on the time variation of the gravitational constant. Methods are based on very diverse physics and the resulting upper bounds differ by several orders of magnitude. Most constraints are obtained from systems in which gravity is non-negligible, such as the motion of the bodies of the Solar system, astrophysical and cosmological systems. They are mainly related in the comparison of a gravitational time scale, e.g. period of orbits, with a non-gravitational time scale. One can distinguish between two types of constraints, from observations from cosmological scales and from local (inner galactic or astrophysical) scales. The strongest constraints to date come from lunar ranging experiments.

In the first column of Table 1 we list the used method. The second column contains the upper bound $|\frac{\Delta G}{G}|_{\text{max}}$ of the fractional change of G during the corresponding timescale. Most of these bound assume a smooth evolution of G . In the third column we present the upper

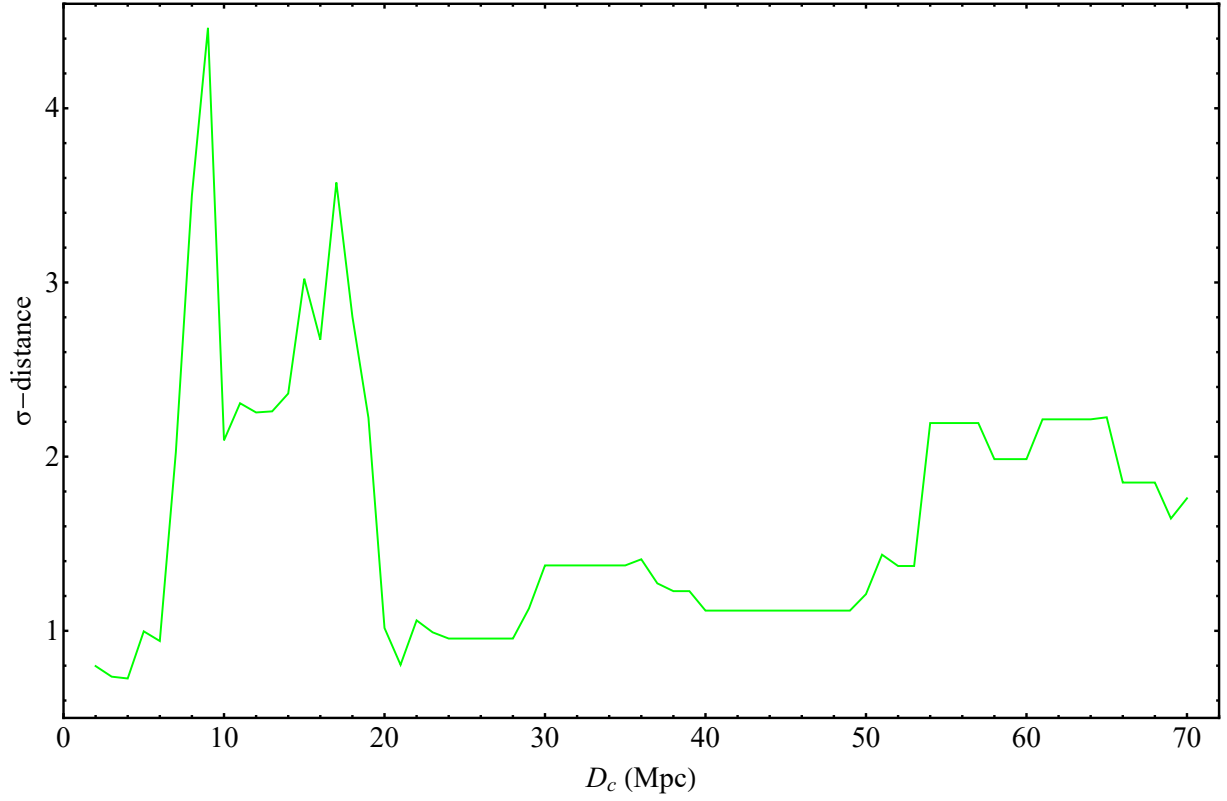


Figure 1. The σ – distance between the various Σ_1 and Σ_2 datasets as a function of the split distances D_c . There are 2 clear peaks at $D_c = 9 \text{ Mpc}$ and $D_c = 17 \text{ Mpc}$ and a transition seems to have been completed at $D_c \approx 20 \text{ Mpc}$. The anticipated plot would have been a σ –distance that consistently varies in the range up to about 2σ for all values of D_c . The observed peaks indicate either the presence of systematics or the presence of interesting physics.

bound on the normalized time derivative $|\frac{\dot{G}}{G}|_{max}$. The fourth column is an approximate time scale over which each experiment is averaging each variation and the fifth column refers to the corresponding study where the bound appears. Entries with a star (*) indicate constraints on G_N while the rest of the constraints refer to the gravitational interaction constant G_N .

In the present analysis we search for a transition of the BTFR best fit parameter values (intercept and slope) between data subsamples at low and high distances for sample dividing distances $D_c \in [2, 60] \text{ Mpc}$ using the robust BTFR dataset of (Lelli et al. 2019, 2016) which consists of 118 carefully selected BTFR datapoints providing distance, rotation velocity baryonic mass (D, V_f, M_b) as well as other observables with their 1σ errorbars. We focus on the gravitational strength Newton constant G_{eff} and address the following questions:

- Are there hints for a transition in the evolution of the BTFR based on recent data?
- What constraints can be imposed on a possible G_{eff} transition using BTFR data?
- Are these constraints consistent with the level of G_{eff} required to address the Hubble tension?

The structure of this paper is the following: In the next section we describe the datasets involved in our analysis, present the method used to identify transitions in the evolution of the BTFR at low z and show the results of our analysis. In Section 3 we summarize, present our conclusions and discuss possible implications and extensions of our analysis.

2 SEARCH FOR TRANSITIONS IN THE EVOLUTION OF THE BTFR

The logarithmic form of the BTFR (eq. (2)) is

$$\log M_B = s \log v_{rot} + \log A_B \equiv s y + b \quad (7)$$

and a similar form for the TFR. Due to eq. (4), the intercept $b \equiv \log A_B$ depends on both the galaxy formation mechanisms through the surface density S and on the strength of gravitational interactions through G_{eff} .

A controversial issue in the literature has been the type of possible evolution of the slope and intercept of the TFR and the BTFR. Most studies have searched for possible evolution in high redshifts (redshift range $z \in [0, 3]$) with controversial results. For example, several studies find no statistically significant evolution of the intercept of the TFR up to redshifts $z \sim 1.7$ (Conselice et al. 2005; Kassim et al. 2007; Müller et al. 2011; Contini, T. et al. 2016; Di Teodoro, E. M. et al. 2016; Molina et al. 2017; Pelliccia, D. et al. 2017) while other studies find a negative evolution of the intercept up to redshift $z \approx 3$ (Puech, M. et al. 2008, 2010; Cresci et al. 2009; Gnerucci, A. et al. 2011; Swinbank et al. 2012; Price et al. 2016; Tiley et al. 2016; Straatman et al. 2017). Similar controversial results in high z appear for the BTFR where (Puech, M. et al. 2010) found no significant evolution of the intercept since $z \approx 0.6$ while (Price et al. 2016) found a positive evolution of the intercept between low- z galaxies and a $z \approx 2$ sample. In addition, cosmological simulations of disc galaxy formation based on cosmological N-body/hydrodynamical simulations have indicated no evolution of the TFR based on stellar masses in the range $z \in [0.1]$ (Portinari & Sommer-Larsen 2007),

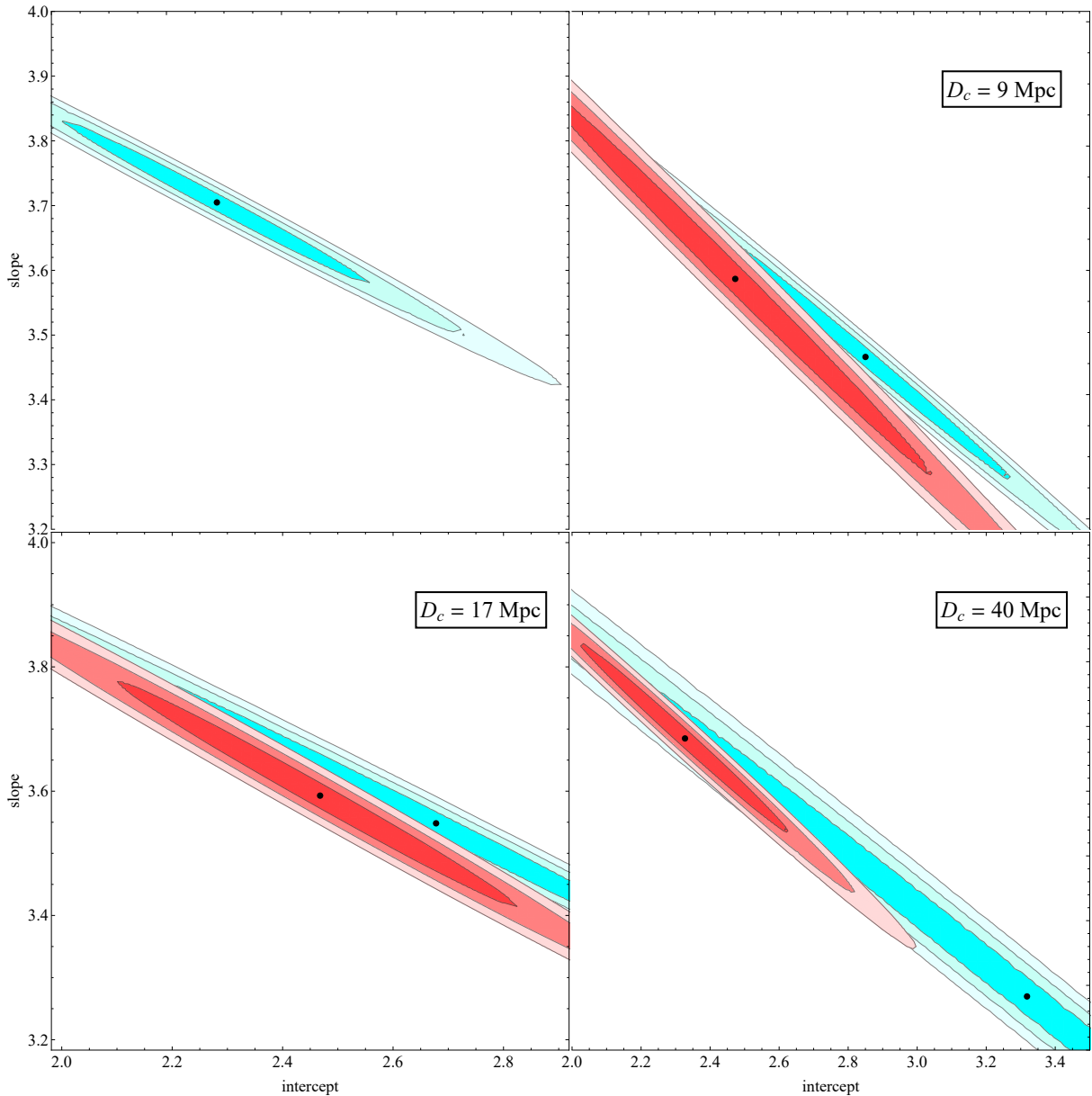


Figure 2. The best fit contours of the slope and intercept for the entire dataset, as well for 3 different cases of split distance (D_c). The red contours correspond to the dataset with galaxies that have distance below D_c , whereas the cyan contours regard galaxies with distances above D_c .

indicating also that any observed evolution of the TFR is an artifact of the luminosity evolution.

These studies have focused mainly on comparing high- z with low- z samples making no attempt to scan low redshift samples for abrupt transitions of the intercept and slope. Such transitions would be hard to explain in the context of known galaxy formation mechanisms but are well motivated in the context of fundamental gravitational constant transitions that may be used to address the Hubble tension (Alestas et al. 2020a; Marra & Perivolaropoulos 2021). Thus, in this section we attempt to fill this gap in the literature.

We consider the BTFR dataset of the updated SPARC database (Lelli et al. 2019, 2016) of flat rotation velocity of galaxies vs the baryonic mass (stars plus gas) consisting of 118 datapoints, shown in Table A1. The sample is restricted to those objects for which both quantities are measured to better than 20% accuracy and includes galaxies in the approximate distance range $D \in [1, 130] \text{ Mpc}$. This

is a robust low z dataset ($z < 0.1$) with low scatter showing no evolution of velocity residuals as a function of the central surface density of the stellar disks.

Our analysis is distinct from previous studies in two aspects:

- We use an exclusively low z sample to search for BTFR evolution.
- We focus on a particular type of evolution, *sharp transitions of the intercept and slope*.

In this context we use the dataset shown in Table A1 of the Appendix (Lelli et al. 2019, 2016), consisting of the distance D , the logarithm of the baryonic mass $\log M_B$ and the logarithm of the asymptotically flat rotation velocity $\log v_{rot}$ of 118 galaxies along with 1σ errors. We fix a critical distance D_c and split this sample in two subsamples Σ_1 (galaxies with $D < D_c$) and Σ_2 (galaxies with $D > D_c$). For each subsample we use the maximum likelihood

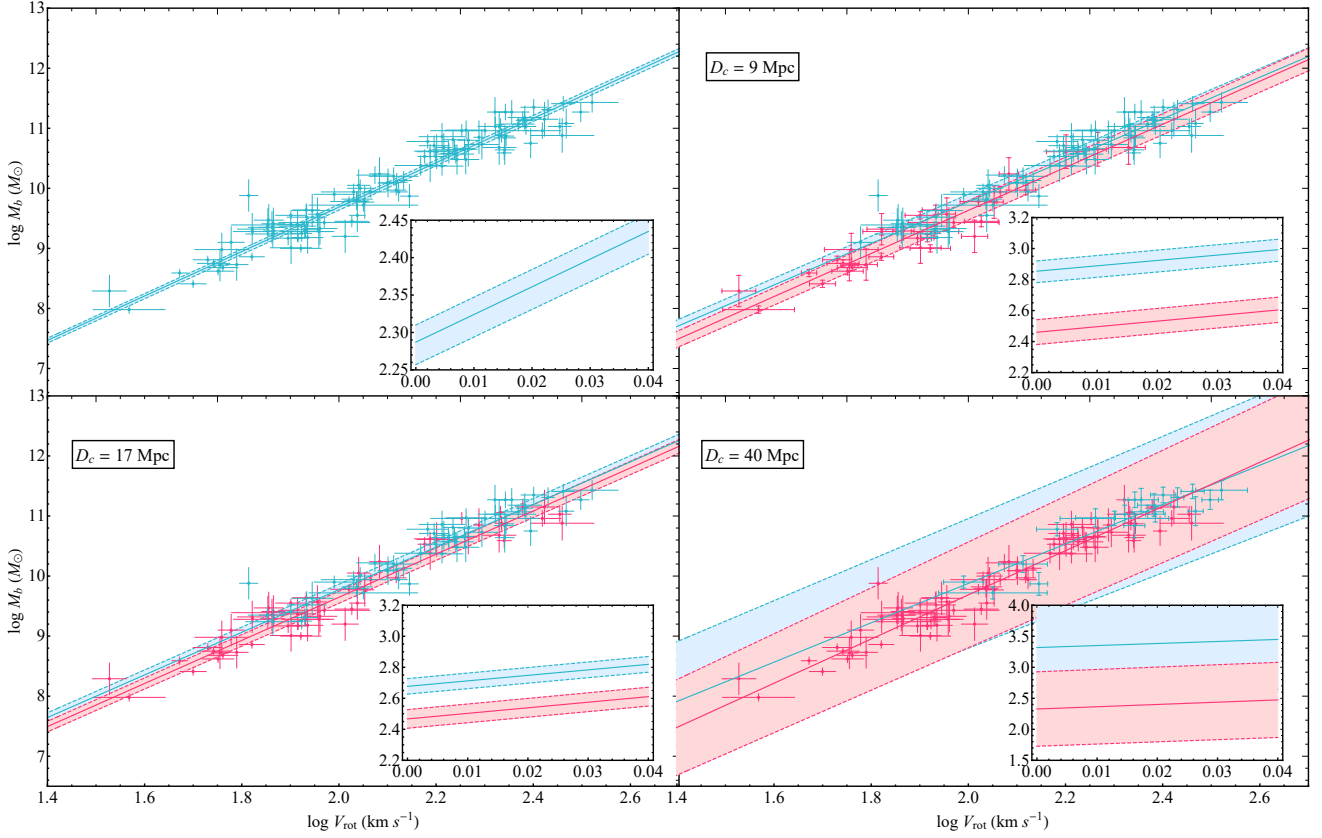


Figure 3. The best fit lines, along with their $1 - \sigma$ region, corresponding to the best fit slope and intercept parameters of the whole galaxy dataset, as well as each of the 2 datasets produced for 4 different split distances (D_c). The red dashed line and datapoints correspond to the data below D_c , and the cyan ones belong to the data over D_c for each case.

D_c (Mpc)	intercept	slope
-	2.287 ± 0.03	3.7 ± 0.01
< 9	2.461 ± 0.08	3.586 ± 0.04
> 9	2.854 ± 0.07	3.46 ± 0.03
< 17	2.467 ± 0.06	3.592 ± 0.02
> 17	2.677 ± 0.05	3.548 ± 0.02
< 40	2.327 ± 0.6	3.681 ± 0.14
> 40	3.318 ± 0.8	3.283 ± 0.14

Table 2. The best fit values of the intercept and slope parameters corresponding to the likelihood contours of Fig. 2 alongside with their 1σ errors.

method (Press et al. 2007) and perform a linear fit to the data setting $y_i = \log(M_B)_i$, $x_i = \log(v_{rot})_i$ while the parameters to fit are the slope s and the intercept b of eq. (7). Thus for each sample j ($j = 0, 1, 2$ with $j = 0$ corresponding to the full sample and $j = 1, 2$ corresponding to the two subsamples Σ_1 and Σ_2) we minimize

$$\chi_j^2(s, b) = \sum_{i=1}^{N_j} \frac{[y_i - (s_j x_i + b_j)]^2}{s_j^2 + \sigma_{x_i}^2 + \sigma_{y_i}^2 + \sigma_s^2} \quad (8)$$

with respect to the slope s_j and intercept b_j . We fix the scatter to $\sigma_s = 0.1$ obtained by demanding that $\frac{\chi_{0,min}^2}{N_0} = 1$ where $\chi_{0,min}^2$ is the minimized value of χ^2 for the full sample and N_0 is the number of data points of the full sample. We thus find the best fit values of the parameters s_j and b_j , ($j = 0, 1, 2$) and also construct the $1\sigma - 3\sigma$ likelihood contours in the $s - b$ parameter space for each

sample (full, Σ_1 and Σ_2) for a given value of D_c . We thus evaluate the $\Delta\chi_{kl}^2(D_c)$ of the best fit of each subsample k best fit with respect to the likelihood contours of the other subsample l . Using these values we also evaluate the σ -distances ($d_{\sigma,kl}(D_c)$ and $d_{\sigma,lk}(D_c)$) and conservatively define the minimum of these σ -distances as

$$d_{\sigma}(D_c) \equiv \text{Min} [d_{\sigma,12}(D_c), d_{\sigma,21}(D_c)] \quad (9)$$

For example for the σ -distance of the best fit of Σ_1 with respect to the likelihood contours of Σ_2 we have

$$\Delta\chi_{12}^2(D_c) \equiv \chi_2^2(s_1, b_1)(D_c) - \chi_{2,min}^2(s_2, b_2)(D_c) \quad (10)$$

and $d_{\sigma,12}$ is obtained as a solution of the equation (Press et al. 2007)

$$\Delta\chi_{12}^2 = 2 Q^{-1} \left[\frac{M}{2}, 1 - \text{Erf} \left(\frac{d_{\sigma,12}}{\sqrt{2}} \right) \right] \quad (11)$$

where Q^{-1} is the inverse regularized incomplete Gamma function, M is the number of parameters to fit ($M = 2$ in our case) and Erf is the error function.

Fig. 1 shows the σ distance $d_{\sigma}(D_c)$ in the parameter space (b, s) as a function of the split sample distance D_c . There are two peaks indicating larger than 3σ difference between the two subsamples at $D_c = 9 \text{ Mpc}$ and $D_c = 17 \text{ Mpc}$. In addition a transition of the σ distance $d_{\sigma}(D_c)$ at $D_c \approx 20 \text{ Mpc}$ is apparent.

The two maxima of d_{σ} are more clearly illustrated in Fig. 2 where the likelihood contours are shown in the parameter space s (slope) - b (intercept) for the full sample (upper left panel) and for three

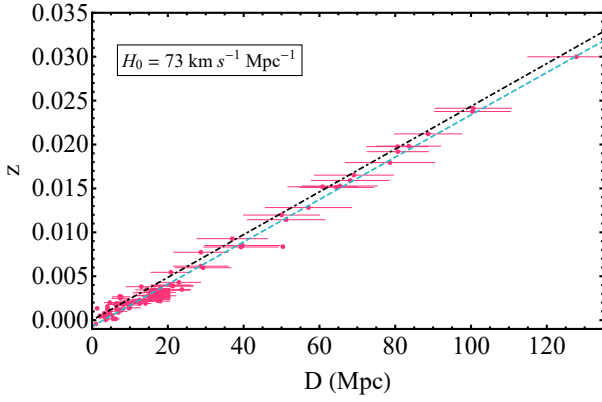


Figure 4. The distances alongside their errorbars versus the redshifts of each galaxy in our compilation. The blue dashed line corresponds to the best fit line, and the black dot dashed one is produced by eq. (2) for $H_0 = 73 \text{ km s}^{-1} \text{ Mpc}^{-1}$.

pairs of subsamples Σ_i including those corresponding to the peaks shown in Fig. 1 ($D_c = 17$ and $D_c = 9$). For both d_σ maxima the tension between the two best fit points is mainly due to the different intercepts while the values of the slope are very similar for the two subsamples. In contrast, for $D_c = 40 \text{ Mpc}$ where the σ distance is much lower (about 1σ , lower right panel) both the slope and the intercept differ significantly in magnitude but the statistical significance of this difference is low.

The statistical significance of the different Tully-Fisher properties between near and far galaxies which abruptly disappears for dividing distance $D_c \gtrsim 20 \text{ Mpc}$ could be a unlikely statistical fluctuation, a hint for systematics in the Tully-Fisher data, an indication for an abrupt change in the galaxy evolution or a hint for a transition in the values of fundamental constants and in particular the strength of gravitational interactions G_{eff} . The best fit values of the intercept and the slope for the cases shown in Fig. 2 are displayed in Table 2 along with their 1σ errors.

The best fit $\log M_B - \log v_{\text{rot}}$ lines corresponding to eq. (7) for the near-far galactic subsamples are shown in Fig. 3 superimposed with the datapoints (red/blue correspond to near/far galaxies). The 1σ error region of the intercept of each line is also shown. The full dataset corresponds to the upper-left panel. The statistical significance of the different intercepts between the two lines for $D_c = 9 \text{ Mpc}$ and $D_c = 17 \text{ Mpc}$ is evident even though their slopes are very similar. This significance disappears for larger values of the splitting distance (e.g. $D_c = 40 \text{ Mpc}$) even though the slopes of the two lines becomes significantly different in this case.

The Hubble diagram of the considered dataset along with the best fit line (black dot-dashed line) and the Hubble blue dashed line ($z \approx \frac{D}{c} H_0$) corresponding to $H_0 = 73 \text{ km s}^{-1} \text{ Mpc}^{-1}$ is shown in Fig. 4. Galaxies closer than about $D \approx 25 \text{ Mpc}$ are clearly not in the Hubble flow and their redshift is affected significantly by their in-falling peculiar velocities which tend to reduce their cosmological redshifts. The detected transition at about 20 Mpc corresponds to a cosmological redshift $z \approx 0.005$ which is lower than the transition redshift required for the resolution of the Hubble tension ($z_t \approx 0.07$ is the upper redshift of SNIa-Cepheid host galaxies).

If the intercept transition at $D_c \approx 20 \text{ Mpc}$ is interpreted as due to a transition of G_{eff} we can use eq. (4) along with the observed intercept transition amplitude shown in Table 2 to identify the magnitude and sign of the corresponding G_{eff} transition. The intercept transition at

$D_c = 17 \text{ Mpc}$ indicated in Table 2 corresponds to

$$\Delta \log A_B \equiv \log A_B^> - \log A_B^< \approx 0.2 \pm 0.06 \quad (12)$$

Since A_B is found to be higher at larger distances (early times), G_{eff} should be lower due to eq. (4). The corresponding fractional change of G_{eff} is easily obtained by differentiating the logarithmic form of eq (4) as

$$\Delta \log A_B = \frac{\Delta A_B}{A_B} = -2 \frac{\Delta G_{\text{eff}}}{G_{\text{eff}}} \implies \frac{\Delta G_{\text{eff}}}{G_{\text{eff}}} \approx -0.1 \pm 0.03 \quad (13)$$

This sign (weaker gravity at early times) and magnitude of the G_{eff} transition is consistent with the gravitational transition required for the resolution of the Hubble and growth tensions in the context of the mechanism of Ref. (Marra & Perivolaropoulos 2021).

3 CONCLUSION-DISCUSSION

We have used a robust dataset of 118 Tully-Fisher datapoints to demonstrate the existence of evidence for a transition in the evolution of BTFR. This evidence appears at a level of more than 3σ and corresponds to a transition of the intercept of the BTFR at a distance $D_c \approx 9 \text{ Mpc}$ and/or at $D_c \approx 17 \text{ Mpc}$ (about 60 million years ago). Such a transition could be interpreted as a transition of the effective Newton constant with a 10% lower value at early times with the transition taking place about 60 million years ago. The amplitude and sign of the gravitational transition are consistent with a recently proposed mechanism for the resolution of the Hubble and growth tensions (Marra & Perivolaropoulos 2021; Alestas et al. 2020a). However, the time of the transition is about 60 million years later than the time suggested by the above mechanism (100-150 million years ago corresponding to $D_c \approx 30-40 \text{ Mpc}$ and $z \approx 0.007-0.01$).

An important extension of this analysis is the search for similar transition signals and constraints in other types of astrophysical and geophysical-climatological data of Earth paleontology. For example a wide range of solar system anomalies have been discussed in Ref. (Iorio 2015) which could be revisited in the context of the gravitational transition hypothesis. Of particular interest for example is the 'Faint young Sun paradox' (Feulner 2012) which involves an inconsistency between geological findings and solar models about the temperature of the Earth about 4 billion years ago.

Alternatively, other astrophysical relations that involve gravitational physics like the Faber-Jackson relation between intrinsic luminosity and velocity dispersion of elliptical galaxies or the Cepheid star period-luminosity relation could also be screened for similar types of transitions as in the case of BTFR. For example, the question to address in Cepheid case would be the following: 'What constraints can be imposed on a transition type evolution of the absolute magnitude (M_V) -period (P) relation of Population I Cepheid stars?' This relation may be written as

$$M_V = s (\log P - 1) + b \quad (14)$$

where $s = -2.43 \pm 0.12$ and $b = -4.05 \pm 0.02$ (Benedict et al. 2007, 2002).

In conclusion the low z gravitational transition hypothesis is weakly constrained in the context of current studies but it could lead to resolution of important cosmological tensions of the Standard Model. We have demonstrated the existence of hints for such a transition in the evolution of the Tully-Fisher relation.

ACKNOWLEDGEMENTS

This research has made use of the SIMBAD database (Wenger et al. 2000), operated at CDS, Strasbourg, France. LP's and GA's research is co-financed by Greece and the European Union (European Social Fund - ESF) through the Operational Programme "Human Resources Development, Education and Lifelong Learning 2014-2020" in the context of the project MIS 5047648.

DATA AVAILABILITY

The galaxy dataset used (Lelli et al. 2019, 2016) can be found in the SPARC database. The distances as well as the redshift data for the majority of the datapoints were taken from the SIMBAD database. The numerical files for the reproduction of the figures can be found in the Tully_Fisher_Transition Github repository under the MIT license.

REFERENCES

- Aaronson M., Huchra J., Mould J., 1979, *Astroph. J.*, 229, 1
- Aghanim N., et al., 2020, *Astron. Astrophys.*, 641, A6
- Alestars G., Perivolaropoulos L., 2021, *Monthly Notices of the Royal Astronomical Society*
- Alestars G., Kazantzidis L., Perivolaropoulos L., 2020a, preprint (arXiv:2012.13932)
- Alestars G., Kazantzidis L., Perivolaropoulos L., 2020b, *Phys. Rev. D*, 101, 123516
- Alvey J., Sabti N., Escudero M., Fairbairn M., 2020, *Eur. Phys. J.*, C80, 148
- Amendola L., Corasaniti P. S., Occhionero F., 1999, preprint (arXiv:astro-ph/9907222)
- Benedict G. F., et al., 2002, *Astron. J.*, 124, 1695
- Benedict G. F., et al., 2007, *Astron. J.*, 133, 1810
- Camarena D., Marra V., 2020, *Mon. Not. Roy. Astron. Soc.*, 495, 2630
- Conselice C. J., Bundy K., Ellis R. S., Brichmann J., Vogt N. P., Phillips A. C., 2005, *Astrophys. J.*, 628, 160
- Contini, T. et al., 2016, *A&A*, 591, A49
- Córsico A. H., Althaus L. G., García-Berro E., Romero A. D., 2013, *JCAP*, 06, 032
- Cresci G., et al., 2009, *Astrophysical Journal*, 697, 115
- Degl'Innocenti S., Fiorentini G., Raffelt G. G., Ricci B., Weiss A., 1996, *Astron. Astrophys.*, 312, 345
- Deller A. T., Verbiest J. P. W., Tingay S. J., Bailes M., 2008, *Astrophys. J. Lett.*, 685, L67
- Di Teodoro, E. M. Fraternali, F. Miller, S. H. 2016, *A&A*, 594, A77
- Di Valentino E., et al., 2021, preprint (arXiv:2103.01183)
- Esposito-Farese G., Polarski D., 2001, *Phys. Rev. D*, 63, 063504
- Feulner G., 2012, *Rev. Geophys.*, 50, RG2006
- Freeman K. C., 1970, *Astroph. J.*, 160, 811
- Freeman K. C., 1999, *Ap&SS*, 269, 119
- Gaztanaga E., Garcia-Berro E., Isern J., Bravo E., Dominguez I., 2002, *Phys. Rev. D*, 65, 023506
- Gaztañaga E., Cabré A., Hui L., 2009, *Monthly Notices of the Royal Astronomical Society*, 399, 1663–1680
- Genova A., Mazarico E., Goossens S., Lemoine F. G., Neumann G. A., Smith D. E., Zuber M. T., 2018, *Nature communications*, 9, 289
- Gnerucci, A. et al., 2011, *A&A*, 528, A88
- Guenther D. B., Krauss L. M., Demarque P., 1998, *The Astrophysical Journal*, 498, 871
- Hellings R. W., Adams P. J., Anderson J. D., Keeseey M. S., Lau E. L., Standish E. M., Canuto V. M., Goldman I., 1983, *Phys. Rev. Lett.*, 51, 1609
- Hofmann F., Müller J., 2018, *Class. Quant. Grav.*, 35, 035015
- Iorio L., 2015, *Int. J. Mod. Phys. D*, 24, 1530015
- Jofre P., Reisenegger A., Fernandez R., 2006, *Phys. Rev. Lett.*, 97, 131102
- Kassin S. A., et al., 2007, *Astrophys. J. Lett.*, 660, L35
- Lelli F., McGaugh S. S., Schombert J. M., 2016, *ApJ*, 816, L14
- Lelli F., McGaugh S. S., Schombert J. M., Desmond H., Katz H., 2019, *MNRAS*, 484, 3267
- Marra V., Perivolaropoulos L., 2021, preprint (arXiv:2102.06012)
- Masuda K., Suto Y., 2016, *Publ. Astron. Soc. Jap.*, 68, L5
- McGaugh S. S., 2005, *The Astrophysical Journal*, 632, 859
- McGaugh S. S., de Blok W. J. G., 1998, *Astrophys. J.*, 499, 41
- McGaugh S. S., Schombert J. M., Bothun G. D., de Blok W. J. G., 2000, *ApJ*, 533, L99
- Miller S. H., Bundy K., Sullivan M., Ellis R. S., Treu T., 2011, *Astrophys. J.*, 741, 115
- Molina J., Ibar E., Swinbank A. M., Sobral D., Best P. N., Smail I., Escala A., Cirasuolo M., 2017, *MNRAS*, 466, 892
- Pelliccia, D. Tresse, L. Epinat, B. Ilbert, O. Scoville, N. Amram, P. Lemaux, B. C. Zamorani, G. 2017, *A&A*, 599, A25
- Pitjeva E. V., Pitjev N. P., 2013, *Mon. Not. Roy. Astron. Soc.*, 432, 3431
- Portinari L., Sommer-Larsen J., 2007, *Mon. Not. Roy. Astron. Soc.*, 375, 913
- Press W. H., Teukolsky S. A., Vetterling W. T., Flannery B. P., 2007, *Numerical Recipes 3rd Edition: The Art of Scientific Computing*, 3 edn. Cambridge University Press, USA
- Price S. H., et al., 2016, *The Astrophysical Journal*, 819, 80
- Puech, M. et al., 2008, *A&A*, 484, 173
- Puech, M. Hammer, F. Flores, H. Delgado-Serrano, R. Rodrigues, M. Yang, Y. 2010, *A&A*, 510, A68
- Riess A. G., Casertano S., Yuan W., Bowers J. B., Macri L., Zinn J. C., Scolnic D., 2021, *Astrophys. J. Lett.*, 908, L6
- Schombert J., McGaugh S., Lelli F., 2020, *Astron. J.*, 160, 71
- Straatman C. M. S., et al., 2017, *The Astrophysical Journal*, 839, 57
- Swinbank M., Sobral D., Smail I., Geach J., Best P., McCarthy I., Crain R., Theuns T., 2012, *Mon. Not. Roy. Astron. Soc.*, 426, 935
- Thorssett S. E., 1996, *Phys. Rev. Lett.*, 77, 1432
- Tiley A. L., et al., 2016, *Monthly Notices of the Royal Astronomical Society*, 460, 103
- Tully R. B., Fisher J. R., 1977, *Astron. Astrophys.*, 54, 661
- Übler H., et al., 2017, *Astroph. J.*, 842, 121
- Uzan J.-P., 2003, *Rev. Mod. Phys.*, 75, 403
- Verheijen M. A. W., 2001, *Astroph. J.*, 563, 694
- Vijaykumar A., Kapadia S. J., Ajith P., 2020, preprint (arXiv:2003.12832)
- Wenger M., et al., 2000, *A&AS*, 143, 9
- Wright B. S., Li B., 2018, *Phys. Rev. D*, 97, 083505
- Wu F., Chen X., 2010, *Phys. Rev. D*, 82, 083003
- Zaritsky D., et al., 2014, *Astron. J.*, 147, 134
- Zhu W. W., et al., 2019, *Mon. Not. Roy. Astron. Soc.*, 482, 3249
- Zwaan M. A., van der Hulst J. M., de Blok W. J. G., McGaugh S. S., 1995, *Mon. Not. Roy. Astron. Soc.*, 273, L35

APPENDIX A: DATASET OF GALAXIES USED

The following is the robust dataset of galaxies used in the analysis. We have used a compilation of 118 datapoints from Ref. (Lelli et al. 2019, 2016) found in the SPARC database, for which M_B , v_{rot} and D were available. Our analysis has been tested by reproducing the corresponding results of (Lelli et al. 2016).

Galaxy Name	$\text{Log}v_{rot}$ (km/s)	$\sigma_{\text{Log}v_{rot}}$ (km/s)	$\text{Log}M_B$ (M_{\odot})	$\sigma_{\text{Log}M_B}$ (M_{\odot})	D (Mpc)	σ_D (Mpc)
D631-7	1.76118	0.0308388	8.68	0.05	7.72	0.39
DDO154	1.6721	0.0156979	8.59	0.06	4.04	0.2
DDO161	1.82151	0.0301116	9.32	0.26	7.5	2.25
DDO168	1.72997	0.0299032	8.81	0.06	4.25	0.21
DDO170	1.77815	0.0267633	9.1	0.26	15.4	4.62
ESO079-G014	2.24304	0.011904	10.48	0.24	28.7	7.17
ESO116-G012	2.03782	0.015912	9.55	0.27	13.	3.9
ESO563-G021	2.49776	0.0169682	11.27	0.16	60.8	9.1
F568-V1	2.05038	0.111688	9.72	0.1	80.6	8.06
F571-8	2.1452	0.0180186	9.87	0.19	53.3	10.7
F574-1	1.99034	0.0412699	9.9	0.1	96.8	9.68
F583-1	1.93349	0.0399604	9.52	0.22	35.4	8.85
IC2574	1.82217	0.0392169	9.28	0.06	3.91	0.2
IC4202	2.38489	0.0200363	11.03	0.13	100.4	10.
KK98-251	1.52763	0.0347715	8.29	0.26	6.8	2.04
NGC0024	2.02653	0.0347037	9.45	0.09	7.3	0.36
NGC0055	1.93247	0.0273785	9.64	0.08	2.11	0.11
NGC0100	1.94498	0.0428581	9.63	0.27	18.45	0.2
NGC0247	2.02078	0.0376492	9.78	0.08	3.7	0.19
NGC0289	2.21219	0.0473939	10.86	0.22	20.8	5.2
NGC0300	1.96988	0.0934984	9.43	0.08	2.08	0.1
NGC0801	2.34262	0.0138028	11.27	0.13	80.7	8.07
NGC0891	2.33465	0.0124516	10.88	0.11	9.91	0.5
NGC1003	2.0406	0.0229253	10.05	0.26	11.4	3.42
NGC1090	2.2159	0.0150474	10.68	0.23	37.	9.25
NGC2403	2.11793	0.0201784	9.97	0.08	3.16	0.16
NGC2683	2.18752	0.0321273	10.62	0.11	9.81	0.49
NGC2841	2.45454	0.0233153	11.03	0.13	14.1	1.4
NGC2903	2.26623	0.0176327	10.65	0.28	6.6	1.98
NGC2915	1.92169	0.0415808	9.	0.06	4.06	0.2
NGC2976	1.93146	0.0487869	9.28	0.11	3.58	0.18
NGC2998	2.32201	0.0196427	11.03	0.15	68.1	10.2
NGC3109	1.82086	0.025568	8.86	0.06	1.33	0.07
NGC3198	2.17638	0.0135896	10.53	0.11	13.8	1.4
NGC3521	2.3298	0.0343219	10.68	0.28	7.7	2.3
NGC3726	2.22531	0.0341	10.64	0.15	18.	2.5
NGC3741	1.69984	0.0268543	8.41	0.06	3.21	0.17
NGC3769	2.07408	0.0373255	10.22	0.14	18.	2.5
NGC3877	2.22634	0.0159786	10.58	0.16	18.	2.5
NGC3893	2.24055	0.0364161	10.57	0.15	18.	2.5
NGC3917	2.13322	0.016287	10.13	0.15	18.	2.5
NGC3949	2.21219	0.0428675	10.37	0.15	18.	2.5
NGC3953	2.344	0.0157246	10.87	0.16	18.	2.5
NGC3972	2.12287	0.0176609	9.94	0.15	18.	2.5
NGC3992	2.38202	0.0167477	11.13	0.13	23.7	2.3
NGC4010	2.09968	0.0189746	10.09	0.14	18.	2.5
NGC4013	2.23779	0.0188259	10.64	0.16	18.	2.5
NGC4051	2.1959	0.0301312	10.71	0.16	18.	2.5
NGC4085	2.11893	0.0214525	10.1	0.15	18.	2.5
NGC4088	2.23477	0.0212324	10.81	0.15	18.	2.5
NGC4100	2.19921	0.0224956	10.53	0.15	18.	2.5
NGC4138	2.1682	0.0530346	10.38	0.16	18.	2.5
NGC4157	2.26647	0.0218527	10.8	0.15	18.	2.5
NGC4183	2.04376	0.0258987	10.	0.14	18.	2.5
NGC4217	2.2584	0.0217838	10.66	0.16	18.	2.5
NGC4559	2.0835	0.0200528	10.24	0.27	7.31	0.2
NGC5005	2.41863	0.0377391	10.96	0.13	16.9	1.5
NGC5033	2.28825	0.0105036	10.85	0.27	15.7	4.7
NGC5055	2.25285	0.0344291	10.96	0.1	9.9	0.5
NGC5371	2.32118	0.0153298	11.27	0.24	39.7	9.92

NGC5585	1.95569	0.0177829	9.57	0.27	7.06	2.12
NGC5907	2.33244	0.0076707	11.06	0.1	17.3	0.9
NGC5985	2.46776	0.0155211	11.08	0.24	50.35	0.2
NGC6015	2.1878	0.0228125	10.38	0.27	17.	5.1
NGC6195	2.40088	0.0260366	11.35	0.13	127.8	12.8
NGC6503	2.06558	0.0123147	9.94	0.09	6.26	0.31
NGC6674	2.38256	0.0343531	11.18	0.19	51.2	10.2
NGC6946	2.20112	0.0404229	10.61	0.28	5.52	1.66
NGC7331	2.3784	0.0112586	11.15	0.13	14.7	1.5
NGC7814	2.34025	0.014275	10.59	0.11	14.4	0.72
UGC00128	2.11261	0.0502315	10.2	0.14	64.5	9.7
UGC00731	1.8651	0.0236835	9.41	0.26	12.5	3.75
UGC01281	1.74194	0.0330217	8.75	0.06	5.27	0.1
UGC02259	1.93551	0.0312158	9.18	0.26	10.5	3.1
UGC02487	2.52114	0.0533349	11.43	0.16	69.1	10.4
UGC02885	2.46165	0.0238363	11.41	0.12	80.6	8.06
UGC02916	2.26174	0.0410958	10.97	0.15	65.4	9.8
UGC02953	2.42308	0.0273605	11.15	0.28	16.5	4.95
UGC03205	2.34163	0.0215419	10.84	0.2	50.	10.
UGC03546	2.29425	0.0337237	10.73	0.24	28.7	7.2
UGC03580	2.10106	0.0192583	10.09	0.23	20.7	5.2
UGC04278	1.96095	0.034663	9.33	0.26	12.59	0.2
UGC04325	1.95856	0.0305567	9.28	0.27	9.6	2.88
UGC04499	1.86213	0.0262308	9.35	0.26	12.5	3.75
UGC05253	2.3298	0.0434609	11.03	0.23	22.9	5.72
UGC05716	1.86392	0.0558085	9.24	0.22	21.3	5.3
UGC05721	1.90146	0.0424743	9.01	0.26	6.18	1.85
UGC05986	2.05308	0.0188195	9.77	0.27	8.63	2.59
UGC06399	1.92942	0.0265506	9.31	0.14	18.	2.5
UGC06446	1.91487	0.0369586	9.37	0.26	12.	3.6
UGC06614	2.3006	0.11165	10.96	0.12	88.7	8.87
UGC06667	1.92324	0.0201981	9.25	0.13	18.	2.5
UGC06786	2.34124	0.0193856	10.64	0.24	29.3	7.32
UGC06787	2.39463	0.0134696	10.75	0.24	21.3	5.32
UGC06818	1.85248	0.0390112	9.35	0.13	18.	2.5
UGC06917	2.03623	0.0247544	9.79	0.14	18.	2.5
UGC06923	1.90091	0.0278065	9.4	0.14	18.	2.5
UGC06930	2.03019	0.0663955	9.94	0.13	18.	2.5
UGC06983	2.03743	0.0310569	9.82	0.13	18.	2.5
UGC07125	1.81425	0.018638	9.88	0.26	19.8	5.9
UGC07151	1.86629	0.0218476	9.29	0.08	6.87	0.34
UGC07399	2.01284	0.026967	9.2	0.27	8.43	2.53
UGC07524	1.90091	0.0310779	9.55	0.06	4.74	0.24
UGC07603	1.78958	0.02325	8.73	0.26	4.7	1.41
UGC07690	1.75891	0.0551951	8.98	0.27	8.11	2.43
UGC08286	1.91593	0.0131675	9.17	0.06	6.5	0.33
UGC08490	1.89542	0.0287125	9.17	0.11	4.65	0.53
UGC08550	1.75511	0.0175431	8.72	0.26	6.7	2.
UGC08699	2.26102	0.0268871	10.48	0.24	39.3	9.82
UGC09037	2.1827	0.0424596	10.78	0.11	83.6	8.4
UGC09133	2.35564	0.0352099	11.27	0.19	57.1	11.4
UGC10310	1.8537	0.0747647	9.39	0.27	15.2	4.6
UGC11455	2.4304	0.013049	11.31	0.16	78.6	11.8
UGC11914	2.45954	0.0650774	10.88	0.28	16.9	5.1
UGC12506	2.36922	0.0324573	11.07	0.11	100.6	10.1
UGC12632	1.85552	0.0296597	9.47	0.26	9.77	2.93
UGCA442	1.75128	0.0323191	8.62	0.06	4.35	0.22
UGCA444	1.5682	0.0738973	7.98	0.06	0.98	0.05

Table A1: A compilation of data from the galaxy dataset of Ref. (Lelli et al. 2019, 2016) found in the SPARC database.